ACS APPLIED MATERIALS & INTERFACES

www.acsami.org

Research Article

Bioinspired Suprahelical Frameworks as Scaffolds for Artificial Photosynthesis

Kai Tao,* Bin Xue,* Shuyi Han, Ruth Aizen, Linda J. W. Shimon, Zhengyu Xu, Yi Cao, Deqing Mei, Wei Wang, and Ehud Gazit*

Cite This: *ACS Appl. Mater. Interfaces* 2020, 12, 45192−45201

Read Online

ACCESS | Metrics & More | Article Recommendations | Supporting Information

ABSTRACT: Framework materials have shown promising potential in various biological applications. However, the state-of-the-art components show low biocompatibility or mechanical instability, or cannot integrate both optics and electronics, thus severely limiting their extensive applications in biological systems. Herein, we demonstrate that amide-based bioorganic building blocks, including dipeptides and dipeptide nucleic acids, can self-assemble into hydrogen-bonded suprahelix architectures of controllable handedness, which then form suprahelical frameworks with diverse cavities. Especially, the cavities can be tuned to be hydrophilic or hydrophobic, and the shortest diagonal distance can be modulated from 0.5 to 1.8 nm, with the volume proportion in the unit cell changing from 5 to 60%. Furthermore, the hydrogen bonding networks result in high mechanical rigidity and semiconductively optoelectronic properties, which allow the utilization of the suprahelical frameworks as supramolecular scaffolds for artificial photosynthesis. Our findings reveal amide-based suprahelix architectures acting as bioinspired supramolecular frameworks, thus extending the constituents portfolio and increasing the feasibility of using framework materials for biological applications.

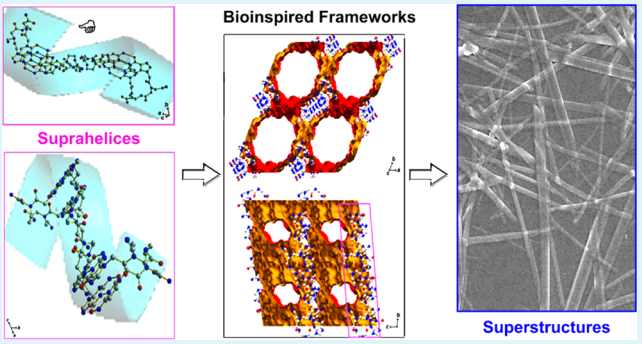

KEYWORDS: *amide-skeleton biomaterials, crystallization engineering, suprahelices, supramolecular frameworks, artificial photosynthesis*

INTRODUCTION

Framework-based materials have attracted increasing interest in diverse well-established fields, such as catalysis, separation, sorption, and storage,[1−5] as well as in the emerging ones including smart microchannels and selective screening-separation in biological systems.[2,3,6] However, conventional inorganic constituents, such as zeolites, have intrinsically low biocompatibility and engineerability, thus severely restricting their uses, especially when interfacing complicated biological systems.[7] Hybrid architectures such as metal−organic frameworks (MOFs) and hydrogen-bonded organic frameworks (HOFs) may ameliorate these shortcomings to some extent. However, their extensive applications are still limited due to several issues, including the involvement of metal ions, restricted biocompatibility, difficulty of morphological or functional modulation, and in many cases, complicated synthesis procedures and mechanical instability.[3,8−13] Recently, several reports demonstrated that biological materials could form supramolecular frameworks by coordination with transition-metal ions (mainly zinc ions).[14−16] Nevertheless, these architectures generally have multiple conformational energy landscape minima, resulting in high sensitivity to external factors (such as solvents and adsorbates) and mechanical instability.[17,18] Therefore, there is a continuing demand for frameworks that can provide flexible modulation and improved properties, along with enhanced eco-friendliness and high structural rigidity.[19−21]

Herein, we demonstrate that amide-based bioinspired components, including dipeptides and dipeptide nucleic acids (diPNAs), can self-assemble into suprahelices, which further associate into supramolecular frameworks with controllable cavities. Furthermore, cavity parameters, including diagonal distances, helical pitches, and hydrophilic nature, can be easily tuned. Especially, the long-range and directional organization of the hydrogen bonds leads to bulky mechanical rigidity and semiconductively photoelectronic characteristics of the suprahelical frameworks, which are further demonstrated to be used as a basis for durable artificial photosynthesis scaffolds. Our findings establish suprahelical frameworks composed of simple bioorganic molecules, thus presenting a new bioinspired

Received: July 23, 2020
Accepted: September 14, 2020
Published: September 14, 2020

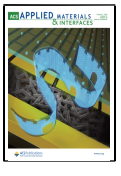

Table 1. Molecular Structures and the Cavity Parameters of the Bioinspired Supramolecular Frameworks

dipeptide

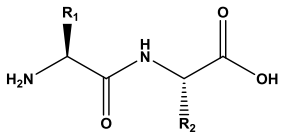

diPNA

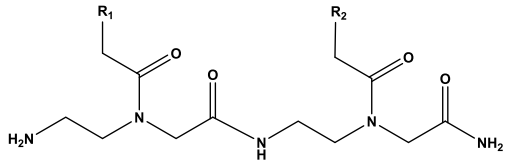

Dipeptide/ diPNA	R_1	R_2	Cavity			
			Hydrophilicity	Shortest diagonal distance (nm)	Volume (A^3)	% in unit cell
FF	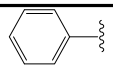	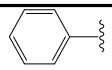	Hydrophilic	1.23	462.87	16.8
VV			Hydrophobic	0.83	271.19	14.4
IV			Hydrophobic	0.74	217.06	11.1
LV			Hydrophobic	0.45	459.93	5.4
diPNA-GC	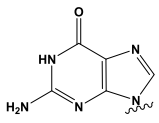	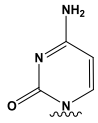	Hydrophilic	1.78 (*c*); 0.90 (*a*)	3660.74	59.4

supramolecular alternative to complement the state-of-the-art counterparts.

RESULTS AND DISCUSSION

Amide-Based Supramolecular Frameworks. Briefly, by combining hydrophobic amino acid side chains to amide backbones to promote aggregation (Table 1), several dipeptides composed of phenylalanine (**F**), valine (**V**), leucine (**L**), and isoleucine (**I**) were designed to crystallize into supramolecular architectures (Table S1 and Figure S3). Crystallographic characterizations demonstrated that only the **FF**,[22] **VV**, **IV**, and **LV** dipeptides formed cavity-containing frameworks (Table 1 and Figure S3).

Scanning electron microscopy (SEM) characterizations demonstrated the large aspect-ratio, rod-like morphologies of the supramolecular architectures (Figures 1A−C and S4A). Crystallographic analyses revealed that the frameworks contained cavities of engineerable hydrophilicity and dimensions (Table 1, Figures 1E−G, and S4B). Specifically, **FF** molecules contributed the two benzyl side chains on the same side of the amide backbone and formed one-dimensional (1-D) hydrophilic channels composed of six monomeric backbones (Figure 1E),[22] showing a shortest diagonal distance of 1.23 nm with a cavity volume of 462.87 $Å^3$ and 16.8% occupation of the unit cell (Table 1). The channels were axially immobilized (along the *c* direction) through 2.88 Å parallel *β*-sheet hydrogen bonds ($N_{amide}\cdots O_{carboxylic}$) between the amide backbones (Figure S5, "1") and connected with each other (along the *ab* plane) by edge-to-face aromatic interactions with dihedral angles of 60−85° (Figure S5, "2"), thus generating an array of hydrophilic channels (Figure 1I). By contrast, in the **VV** system, the two isopropyl side chains were distributed on the opposite sides of the amide backbone and composed hydrophobic 1-D channels (Figure 1F), showing a shortest diagonal distance of 0.83 nm with a cavity volume of 271.19 $Å^3$ and 14.4% occupation of the unit cell (Table 1). The channels were connected with each other (along the *ab* plane) through three hydrogen bonds of 2.71 Å ($N_{amino}\cdots O_{carboxylic}$), 2.98 Å ($N_{amide}\cdots O_{carboxylic}$), and 2.79 Å ($N_{amino}\cdots O_{amide}$) (Figure S6), thus forming an array of hydrophobic channels (Figure 1J).

Intriguingly, the **IV** dipeptide formed supramolecular frameworks similar to **VV** (Figure S4), producing arrays of hydrophobic channels with a shortest diagonal distance of 0.74 nm and a cavity volume of 217.06 $Å^3$ with 11.1% occupation of the unit cell (Table 1). Simultaneously, the channels were connected through hydrogen bonds of 2.73 Å ($N_{amino}\cdots O_{carboxylic}$), 2.97 Å ($N_{amide}\cdots Ode_{carboxylic}$), and 2.80 Å ($N_{amino}\cdots O_{amide}$) (Figure S7, "1"). These findings demonstrate that the replacement of the side-chain isopropyl group to a *sec*-butyl group did not disturb the subtle force equilibrium and allowed to retain the channel conformations, indicating that to some extent, the frameworks could counterbalance the variation of steric hindrance. In contrast, when substituting the *sec*-butyl group with an isobutyl one, as in the **LV** dipeptide, the minor shift of the methyl group to the cavity center in the side chain resulted in significant spatial hindrance and decreased the size of the cavity. To offset this energy perturbation, the cavity conformation significantly transformed. As shown in Figure 1G, in the **LV** system, the 1-D channels disappeared and a six-petal Hong Kong orchid tree-like void was formed instead, with a shortest diagonal distance of 0.45 nm and a cavity volume of 459.93 $Å^3$ with 5.4% occupation of the unit cell

https://dx.doi.org/10.1021/acsami.0c13295
ACS Appl. Mater. Interfaces 2020, 12, 45192−45201

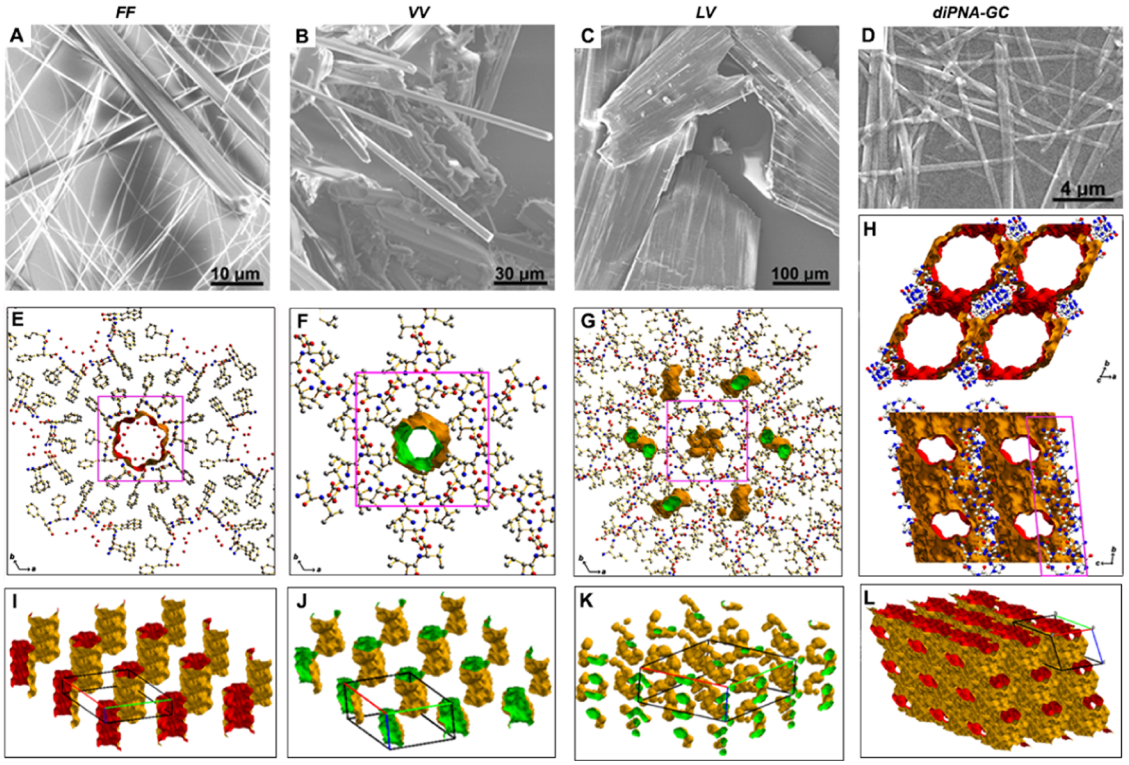

Figure 1. Morphology and cavity characterizations of the bioinspired supramolecular frameworks. (A, E, I) **FF**; (B, F, J) **VV**; (C, G, K) **LV**; (D, H, L) diPNA-**GC**. (A–D) Scanning electron microscopy images of the supramolecular frameworks. (E–H) Crystallographic images showing the molecular organizations comprising the cavities of the frameworks. The magenta quadrangles indicate the suprahelix structures. The colored graphics denote the cavities (channels or voids) inside the frameworks, with the hydrophilic and hydrophobic cavities designated in red and green, respectively. In (H), two views, (top) along the *c* direction and (bottom) along the *a* direction of the channels inside the diPNA-**GC** frameworks, are shown. (I–L) Schematic graphics showing the cavity arrays inside the frameworks. The hexahedrons represent the unit cell axes of the crystals.

(Table 1), significantly smaller than those of the **VV** or **IV** cavities. Particularly, the central large void was further surrounded by six relatively narrower ones, each formed by two alternating circles (Figure S8). This resulted in a bulky distribution of discrete voids in the frameworks (Figure 1K). The two circles were both mediated by hydrogen bonds among the six **LV** monomers. In one circle, the six side-chain isopropyl groups pointed inside by forming two groups of hydrogen bonds of 2.77, 2.74 and 2.72 Å at the terminal carboxyl and amino groups between adjacent monomers, herein termed the "**V** circle" (Figure S8, "1"). By contrast, in the other circle, the six isobutyl moieties were directed inside with four water molecules participating in the circulation by forming two pairs of hydrogen bonds of 2.78 Å ($N_{amino}\cdots O_{carboxylic}$), 2.66 Å ($N_{amino}\cdots O_{water}$), 2.67 Å ($O_{water}\cdots O_{water}$), 2.74 Å ($O_{water}\cdots O_{carboxylic}$), and 2.75 Å ($N_{amino}\cdots O_{carboxylic}$), thus designated the "**L** circle" (Figure S8, "2"). The two circles were tightly linked through extensive hydrogen bonding networks (Figure S9), thus counterbalancing the steric hindrance derived from the methyl group shifting and stabilizing the frameworks.

Considering the role of hydrogen bonding in the formation of amide-based supramolecular architectures,[23,24] the close contacts of the relevant elements (oxygen and nitrogen atoms) were further investigated via Hirshfeld surface analysis (Figure S10).[25] Figure 2 demonstrates that oxygen atoms mostly contributed to the hydrogen bond formation in the dipeptides-based suprahelical frameworks, with the hydrogen bonds formed by nitrogen atoms found to be negligible. Also, the two-dimensional (2-D) fingerprint plots were nearly mirrored

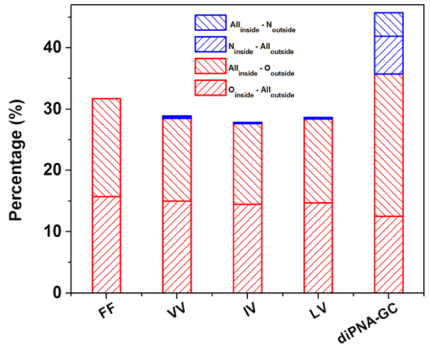

Figure 2. Statistics of the close contact of elements of the suprahelical frameworks from the 2-D fingerprint plots of the Hirshfeld surface. The red and blue bars indicate oxygen and nitrogen atoms, respectively.

along the $d_e = d_i$ division line (Figure S10), resulting in similar O_{inside}–$All_{outside}$ and All_{inside}–$O_{outside}$ ratios, thus indicating the reciprocal O_{inside}–$All_{outside}$ (All_{inside}–$O_{outside}$) contacts.

We aimed to introduce additional hydrogen bonding interactions, especially at the side chains, to develop supramolecular frameworks with larger cavities. Therefore, a PNA with complementary nucleobases as the side chains was synthesized using an Fmoc solid-phase synthesis strategy (see Materials and Experimental Section) to self-assemble into supramolecular structures.[26] Given the robust propensity of nucleobases to form Watson–Crick hydrogen bonding interactions, PNA-based building blocks have been reported to organize into supramolecular architectures significantly

https://dx.doi.org/10.1021/acsami.0c13295
ACS Appl. Mater. Interfaces 2020, 12, 45192–45201

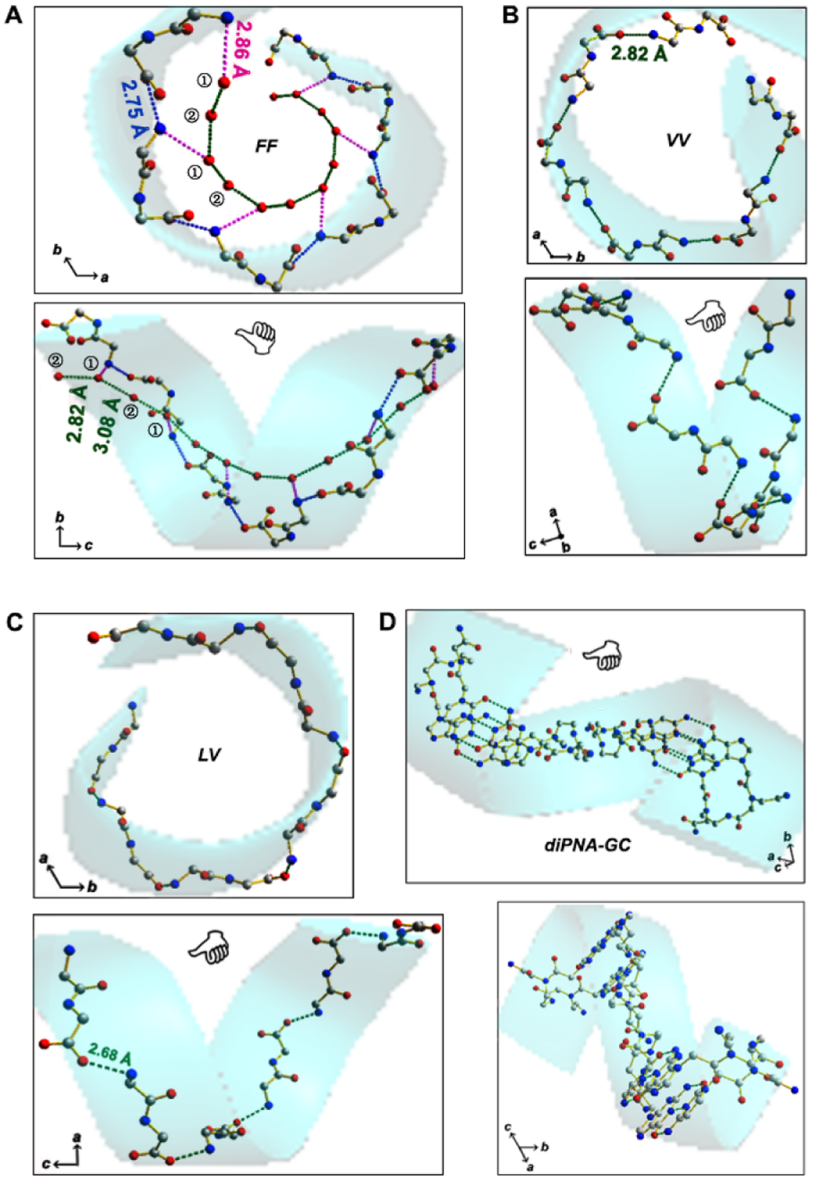

Figure 3. Illustrative depiction of the helix conformations underlying the suprahelical frameworks. (A–C) A pitch of (A) **FF** left-handed, (B) **VV**, and (C) **LV** right-handed suprahelices from a (top) front and (bottom) lateral view. (D) A pitch of diPNA-**GC** right-handed suprahelix viewed from two different directions. The carbon, oxygen, and nitrogen atoms are designated in gray, red, and blue, respectively; the hydrogen atoms and side chains are neglected for clarity. The dotted lines represent the hydrogen bonds; the colors distinguish different groups, with the bond length values labeled in the corresponding colors. In (A), the two types of water molecules participating in crystallization and playing different roles are numerically marked.

distinct from those formed by the peptide-based counterparts.[27−29] We previously reported that diPNA-Guanine-Cytosine (diPNA-**GC**) could self-assemble into 1-D optoelectronic architectures.[29] Crystallographic characterization demonstrated that Watson−Crick base pairing interactions were formed between the side-chain **G** and **C** moieties, with three hydrogen bonds of 2.82 Å (N_C−O_G), 2.91 Å (N_G−N_C), and 2.85 Å (N_G−O_C) (Figure S11, "2"). Combined with the parallel-displaced aromatic interactions of 3.46 and 3.49 Å along the axial direction (*c* direction, Figure S11, "1"),[29] the synergy of these interactions resulted in the amide backbones distributed outwards (Figure S11, "3"), thus constructing multichannel frameworks (Figure 1H), with a shortest diagonal distance of 1.78 nm along the *c* direction and 0.90 nm along the *a* direction (Table 1). This resulted in a significantly high cavity volume of up to 3660.74 A^3 and 59.4% occupation of the unit cell (Table 1). The 2-D fingerprint plots from the Hirshfeld surface analysis demonstrate that new contacts (peaks) emerged in the diPNA-**GC** crystals compared to the dipeptide-based counterparts (Figure S12). Especially, the nitrogen elements significantly contributed to the hydrogen bonding interactions, with a total 10.0% ratio, along with 35.7% for oxygen atoms (Figure 2). These results confirmed the interactions between individual diPNA-**GC** molecules had been strengthened compared to the dipeptide counterparts,[30] thus demonstrating that the introduction of hydrogen bonding at the side chains can indeed develop frameworks with larger cavities.

Suprahelix Underlying the Supramolecular Frameworks. Intriguingly, the cavities inside the supramolecular frameworks were composed of hydrogen-bonded helical structures, as shown in Figure 3. However, the helix

https://dx.doi.org/10.1021/acsami.0c13295
ACS Appl. Mater. Interfaces 2020, 12, 45192−45201

configurations, including the handedness, pitch length, and number of monomers per pitch, varied among the different frameworks (Figure 3and Table 2). Especially, the supra-

Table 2. Summary of the Helical Parameters of the Bioinspired Suprahelical Frameworks

building block	handedness	pitch (nm)	no. of monomers/pitch
FF	left	3.28	6
VV	right	1.03	6
IV	right	1.03	6
LV	right	2.34	6
diPNA-**GC**	right	3.34	4

molecular helices were formed through head (amino)-to-tail (carboxylic) hydrogen bonding of six monomers in the peptide systems, in contrast to Watson−Crick hydrogen bonding through four side-chain nucleobases in the diPNA assemblies (Figure 3). Specifically, in the **FF** system, six peptide molecules interacted through the carboxylic and amino groups with a 2.75 Å hydrogen bond ($N_{amino}\cdots O_{carboxylic}$) (Figure 3A, blue dotted lines), thus forming a left-handed supramolecular helix with a pitch of 3.28 nm (Table 2).[23,31] In addition, each **FF** monomer connected with a water molecule (Figure 3A, marked with "①") with a hydrogen bond of 2.86 Å ($N_{amino}\cdots O_{water}$) (Figure 3A, magenta dotted lines). Another water molecule (Figure 3A, marked with "②") served to bridge the water ① molecules, thus forming a helix of water molecules inside the channel with two types of hydrogen bonds, 2.82 Å ($O_①-O_②$) and 3.08 Å ($O_②-O_①$) (Figure 3A, green dotted lines).[32] This structure is consistent with the hydrophilic nature of the **FF** channels. In contrast, the helix compositions of the hydrophobic channels were relatively simpler, showing only head-to-tail, right-handed hydrogen bonds (Table 2). The **VV** and **IV**-based suprahelices were organized by 2.82 and 2.83 Å hydrogen bonds ($N_{amino}\cdots O_{carboxylic}$), respectively (Figures 3B and S7, "1"), forming the same pitch of 1.03 nm (Table 2), while the **LV** suprahelices were organized by a 2.68 Å hydrogen bond ($N_{amino}\cdots O_{carboxylic}$) (Figure 3C) with a pitch of 2.34 nm (Table 2). Nevertheless, in contrast to the peptides, the diPNA-**GC**-based suprahelix showed right-handedness with a large pitch of 3.34 nm albeit the presence of only four monomers per pitch (Table 2 and Figure 3D), since both the backbone and side chains contributed to suprahelix formation.

Mechanical Rigidity of the Suprahelical Frameworks. A long-range hydrogen bonding network can result in high mechanical rigidity.[32−35] For example, the well-studied β-sheet-based proteinaceous nanofibers self-assembled by the amyloid-β polypeptides, as well as ultrashort peptide crystals, can show Young's moduli of 1−30 GPa (Figure 4A, magenta dashed-line region).[35−39] However, several studies reported that helix-containing peptide assemblies, such as coiled-coil architectures, present significantly higher mechanical rigidity.[40−42] Therefore, we examined the mechanical properties of the suprahelical frameworks using atomic force microscopy nanoindentation. The statistical analysis revealed these supramolecular architectures to display Young's moduli of 6−40 GPa (Figure 4A, red dashed-line region, Figure S13). Correspondingly, their point stiffness values were in the range of 90−190 N m^{-1} (Figures 4B and S14). Specifically, the diPNA-**GC** assemblies showed the highest value, with a measured Young's modulus of up to 37.4 ± 7.5 GPa and point stiffness of 183.5 ± 56.9 N m^{-1}, thus confirming that the helix-based conformations are more expedient for mechanical applications than the state-of-the-art β-sheet-based counterparts.[42] Notably, the mechanical rigidity of the suprahelical frameworks is between those of inorganic zeolite (usually higher than 30 GPa)[43] and hybrid MOFs (usually lower than 30 GPa)[44−46] (Figure 4A), thus supplying a new type of bioinspired alternative to bridge the gap. Nevertheless, it should be noted that the temperature can affect the bioinspired frameworks.[47,48] For example, when heating to 250 °C, the **FF** crystals converted into to cyclic-**FF** ones, as confirmed by X-ray diffraction (XRD) and SEM characterizations (Figure S15). Therefore, to be suitable for high-temperature applications, the thermal stability of the suprahelical frameworks should be further enhanced, for instance by increasing the hydrogen bonding interactions.[49]

Suprahelical Frameworks as Bioinspired Scaffolds for Artificial Photosynthesis. The cavity nature and high mechanical rigidity suggest the suprahelical frameworks as candidate supramolecular scaffolds for biocatalytic applications.[50] A Brunauer−Emmett−Teller (BET) measurement demonstrated the apparent average pore diameter to be 2.5−3.5 nm (Table S2) for the various assemblies, consistent with the crystallographic data presented above, with the pore volume ranging from 0.008 to 0.14 cm^3 g^{-1}. Correspondingly, the specific surface area was measured to be 12.40 m^2 g^{-1} for **IV** to 68.1 m^2 g^{-1} for diPNA-**GC** (Table S2). The results

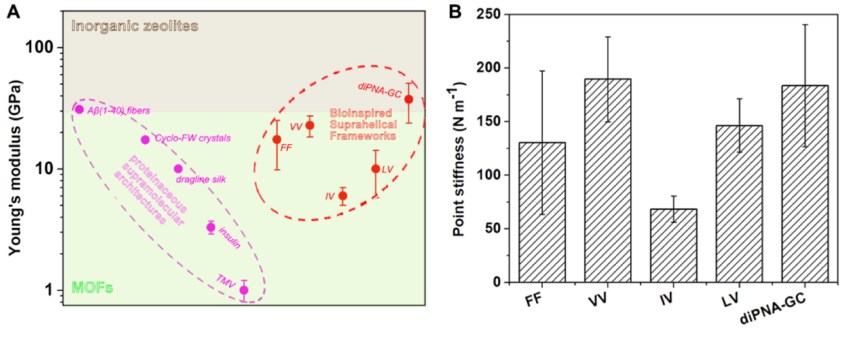

Figure 4. Mechanical properties of the bioinspired suprahelical frameworks. (A) Comparison of Young's moduli of peptide-based supramolecular materials and state-of-the-art porous counterparts. The magenta and red dashed-line frameworks label the regions of the characteristic β-sheet-based peptide self-assembled materials and the suprahelical frameworks, respectively. Young's modulus data: Inorganic zeolites, ref 43; MOFs, ref 44; Aβ(1−40) fibers, ref 39; Cyclo-FW crystals, ref 32; dragline silk and insulin, ref 33; tobacco mosaic virus (TMV) nanotubes, ref 38. (B) Point stiffness statistics for the examined suprahelical frameworks, as indicated.

https://dx.doi.org/10.1021/acsami.0c13295
ACS Appl. Mater. Interfaces 2020, 12, 45192−45201

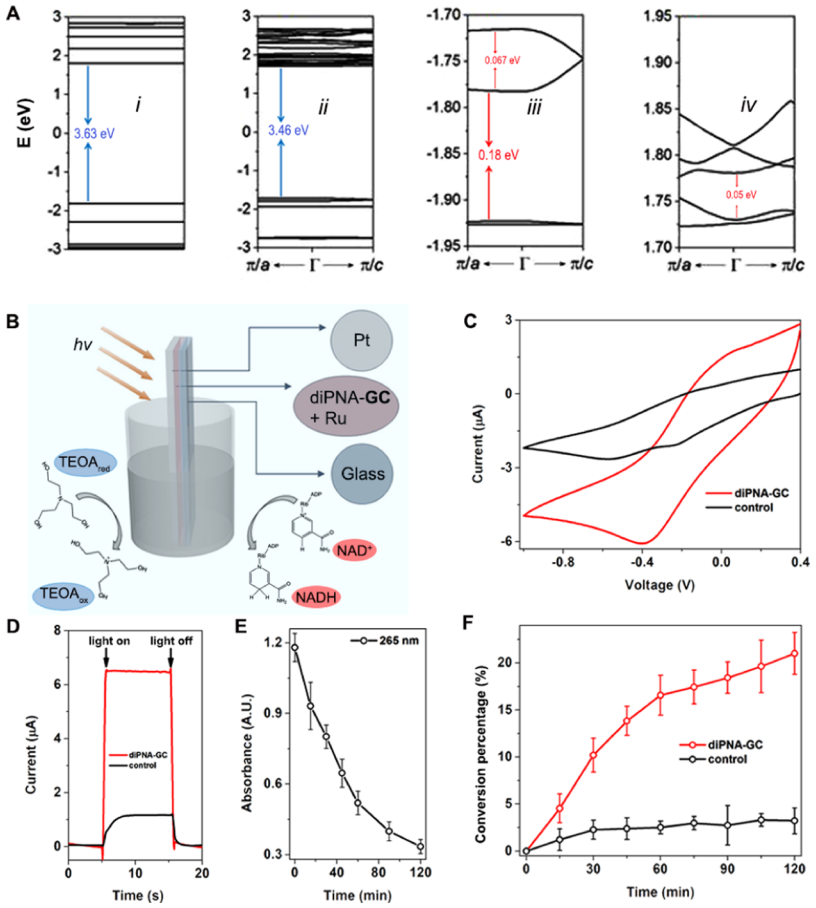

Figure 5. Artificial photosynthesis using the diPNA-**GC**-based suprahelical frameworks as the scaffolds. (A) Band structures (calculated with the HSE06 functional) for (i) diPNA-**GC** single molecule, (ii) diPNA-**GC** crystal near the Fermi level, (iii) diPNA-**GC** crystal valence bands near the Fermi level, and (iv) diPNA-**GC** crystal conduction band near the Fermi level. The band gap values are labeled at the corresponding places. (B) Schematic representation of the artificial photosynthesis configuration. (C) Cyclic voltammogram of $Ru(bpy)_3Cl_2$. (D) Photocurrent response and (E) time-resolved photoinduced UV absorption at 265 nm of nicotinamide adenine dinucleotide (NAD^+) in the presence of the diPNA-**GC** frameworks. (F) Conversion percentage of reduced nicotinamide adenine dinucleotide (NADH) in the presence of the artificial photosynthesis system shown in (B). In (C, D, F), the same experiments without the suprahelical frameworks are shown as controls.

demonstrate the relatively small porous characteristic of the supramolecular scaffolds.[21,22] We further focused on the diPNA-**GC**-based framework due to its higher porous fraction and mechanical rigidness (Figure S16). The extensive hydrogen bonding network can reduce the band gap of peptide assemblies, thus resulting in semiconductively optoelectronic features.[23,51] Therefore, the band structures were first calculated for computationally optimized diPNA-**GC** crystal frameworks (Figure 5A). Compared to 3.63 eV for the single molecule (Figure 5A-i), the band gap for the crystallized structure was 3.46 eV (Figure 5A-ii), thus confirming that the hydrogen bonding organization indeed decreased the electron transfer energy barriers and establishing the diPNA-**GC** assemblies as supramolecular, wide-gap semiconductors.[32,51] Furthermore, we plotted the crystal band structure along *a* from Γ to π/a and along *c* from Γ to π/c. The highest occupied molecular orbital of the diPNA-**GC** molecule in the crystal was split into four energy levels at the Γ point (Figure 5A-iii). Interestingly, the four energy levels could be further divided into two groups with an energy separation of 0.18 eV, each group composed of two bands and the upper levels separated by 0.067 eV (Figure 5A-ii), as a result of the **G**-**C** Watson–Crick interactions. Similarly, the lowest unoccupied molecular orbital in the crystalline structure was also split into several energy bands, with band dispersions within 0.05 eV along both the *c* and *a* direction (Figure 5A-iv). Therefore, the intrinsic wide-gap semiconductivity nature and the delicate band splitting with ultrasmall energy differences led to the wide-spectrum photon-electron transformation of the diPNA-**GC** frameworks, as further confirmed by fluorescent microscopy characterizations (Figure S17).

To examine whether the diPNA-**GC** frameworks could facilitate photoelectron production and transfer,[52,53] an artificial photosynthesis prototype was developed using the diPNA-**GC**-based frameworks as the skeleton structures (Figure 5B). Cyclic voltammetry characterization demonstrated that the suprahelical architectures showed a notable catalytic property for electro-redox of tris(2,2′-bipyridyl)-dichlororuthenium(II) hexahydrate ($Ru(bpy)_3Cl_2{\cdot}6H_2O$), which generally acts as the electron mediator in photosynthesis systems,[54] with a reduction potential peak of −0.39 V, compared to −0.58 V for the control (Figure 5C), illustrating the significant electron transfer ability of the frameworks. Furthermore, photocurrent measurements using triethanolamine (TEOA) as an electron donor illustrated that an indium tin oxide (ITO) glass slide coated with a ruthenium-complex-containing diPNA-**GC** crystal powder could produce a remarkably high photocurrent upon irradiation by a 350 W

https://dx.doi.org/10.1021/acsami.0c13295
ACS Appl. Mater. Interfaces 2020, 12, 45192−45201

Xe lamp (Figure 5D), showing a value 6.5-fold higher (6.5 μA) than that produced by the control ruthenium-complex-coated ITO slide (1.0 μA). This result demonstrates that the suprahelical frameworks can facilitate the delocalization of excitons and suppress electron−hole recombination during photoelectrons production, consistent with the electron level analysis. The UV−vis absorption characterization demonstrated that the concentration of NAD^+ significantly decreased over time in the presence of diPNA-**GC** crystals mixed with $Ru(bpy)_3Cl_2$ under illumination (Figure 5E), thus indicating the feasibility of utilizing the suprahelical framework-supported photosensitizers as the sunlight-sensitive antennas to produce NADH, which is required in many biocatalytic redox reactions.[50,54] Finally, after sputtered with Pt nanoparticles (NPs) as the catalytic centers, the hybrid system (diPNA-**GC**/Ru/Pt) presented a remarkable catalytic activity of NADH regeneration, showing a yield of ∼21% after 2 h, approximately 7-fold higher than the Ru/Pt control (Figure 5F). As additional controls, artificial photosynthesis systems were constructed employing other suprahelical frameworks with lower cavity ratios as the scaffolds, showing reduced efficiency compared to diPNA-**GC** (Figure S18). Furthermore, the mechanical rigidity promoted easy retrieval of the diPNA-**GC** frameworks for storage and reusability, with approximately 50% NADH conversion yield after five cycles without obvious detachment from the substrate (Figure S19). Especially, XRD and SEM characterizations demonstrated that after recycling, the frameworks still kept intact (Figure S16), thus implying the stability of the crystals and potentially allowing to reduce costs and contaminations.

CONCLUSIONS

In summary, we demonstrate that amide-based bioinspired building blocks, including dipeptides and diPNAs, can self-assemble into hydrogen-bonded suprahelices, which finally form suprahelical frameworks. Especially, the extensive and directional hydrogen bonds endowed the frameworks high mechanical rigidity, thus bridging the gap between rigid but nonbiocompatible zeolites and instable hybrid MOFs or HOFs. The intrinsic semiconductively optoelectronic properties endow the suprahelical frameworks the ability to be used as durable skeletons to support photosensitizers and catalysts, along with prompting photoelectron production and transfer for artificial photosynthesis.

Considering the diversity of the amino acid side chains and the nucleotide bases, as well as the intrinsic chirality and the feasibility of chemical or physical modifications of the monomers, the amide-based assembly strategy can be engineered to design suprahelices with unique properties, thus extending the constituents repertoire of cavity-containing materials. Moreover, the bioinspired suprahelical frameworks can be explored for additional applications, such as biomimetic, smart microchannels, and selective screening-separation, thus expanding the applications of bioorganic supramolecular frameworks. Our work demonstrates, for the first time, the structural basis underlying amide-based supramolecular frameworks, thus supplying an alternative conceptual design for preparing and modulating bioinspired frameworks.

MATERIALS AND EXPERIMENTAL SECTION

Materials. The dipeptides were purchased from Bachem (Bubendorf, Switzerland), GL Biochem (Shanghai, China), or DgPeptides (Hangzhou, China). N-terminal and side-chain-protected PNA monomers (Fmoc-PNA-**G**(Bhoc)-OH, Fmoc-PNA-**C**(Bhoc)-OH) were purchased from Polyorg (Leominster, MA), *O*-(1*H*-benzotriazole-1-yl)-*N*,*N*,*N*′,*N*′-tetramethyluronium hexafluorophosphate (HBTU) and *N*-hydroxybenzotriazole anhydrous (HOBt) from Chem-Impex International (Wood Dale, IL), *N*,*N*′-diisopropylethylamine (DIEA) and triisopropylsilane (TIS) from Sigma-Aldrich (Rehovot, Israel), Rink Amide MBHA resin from Merck (Darmstadt, Germany), trifluoroacetic acid (TFA), dichloromethane (DCM), and *N*,*N*-dimethylformamide (DMF) of peptide synthesis purity grade from Bio-Lab (Jerusalem, Israel), tris(2,2′-bipyridyl)-dichlororuthenium(II) hexahydrate ($Ru(bpy)_3Cl_2{\cdot}6H_2O$) and nicotinamide adenine dinucleotide (NAD^+) from Aladdin (Shanghai, China), and triethanolamine (TEOA) from Sinopharm (Shanghai, China). All materials were used as received without further purification. Water was processed by a Millipore purification system (Darmstadt, Germany) with a minimum resistivity of 18.2 MΩ cm.

DiPNA-GC Synthesis. The diPNA-**GC** was synthesized using the standard Fmoc solid-phase synthesis method.[29] After deprotection of the MBHA resin with 20% piperidine and 0.1 M HOBt in DMF, Fmoc-PNA-**C**(Bhoc)-OH was introduced for coupling, followed by introduction of Fmoc-PNA-**G**(Bhoc)-OH. The carboxylic groups were activated by treatment with HBTU/HOBt/DIEA, transforming the carboxylic acids into activated esters to react with the deprotected α-amine groups. After synthesis, cleavage from the resin and deprotection of the side chains were co-performed using a mixture of TFA, TIS, and H_2O at a ratio of 95:2.5:2.5. The cleavage mixture and subsequent DCM washing solution were then purged with nitrogen. The obtained concentrated solutions were added to water and lyophilized. The product identity was verified by electrospray ionization time-of-flight mass spectrometry and reversed-phase high-performance liquid chromatography (Figures S1 and S2).

Crystals Preparation. The dipeptides or the synthesized diPNA-**GC** powders were added to water or commercial 1.0 M BICINE buffer at pH 9.0 (Hampton Research, CA). The solutions were heated in a water bath at 80 °C for 5 min to ensure the complete dissolution of the solutes, followed by filtration using a 0.45 μm PVDF membrane (Merck Millipore, Carrigtwohil, Ireland). The filtered solutions were placed at room temperature and needle-like crystals appeared at the bottom of the vials after several hours and reached maximal size after 30 days. The supernatants were removed and the crystals were washed with water three times and collected for later use.

Scanning Electron Microscopy (SEM). The solution containing the crystals was placed on a clean glass slide, allowed to adsorb for a few seconds and excess liquid was removed with filter paper. The slide was then coated with Cr and observed under a JSM-6700 field emission scanning electron microscope (JEOL, Tokyo, Japan) operated at 10 kV.

X-ray Crystallography. A single crystal suitable for X-ray diffraction was coated with Paratone oil (Hampton Research, CA), mounted on a MiTeGen loop and flash frozen in liquid nitrogen. Diffraction data were measured with Cu Kα radiation at 100(2) K using a Rigaku XtaLabPro with a Dectris PilatusR 200K-A detector. The data were processed using CrysAlisPro 1.171.39.22a. The structures were determined by direct methods using SHELXT-2013 and SHELXT-2016/4 and refined by full-matrix least squares against F2 with SHELXL-2013 and SHELXL-2016/4. All nonhydrogen atoms were refined aniostropically. Hydrogen atoms were placed in calculated positions and refined in riding mode. The SQUEEZE protocol of Platon was implemented for the LI structure due to disordered solvent cavities. The crystal data (cif. files) have been deposited with the CSD (Table S1).

Young's Modulus Measurement. Atomic force microscopy (AFM) experiments were carried out using a commercial AFM (JPK, Nanowizard II, Berlin, Germany). The force curves were obtained using the commercial software from JPK and analyzed by a custom-written procedure based on Igor pro 6.12 (Wavemetrics, Inc.). Silica cantilevers (RTESPA-525 Bruker Company with the half-open angle of the pyramidal face of $\theta < 10°$, tip radius: ∼8 nm, frequency in air: ∼525 kHz) were used in all experiments. The spring constant of the cantilevers was ∼200 N m^{-1}. The maximum loading force was set at

https://dx.doi.org/10.1021/acsami.0c13295
ACS Appl. Mater. Interfaces 2020, 12, 45192−45201

800 nN. All AFM experiments were carried out at room temperature. In a typical experiment, the crystal samples were cast on the surface of the glass substrate and the cantilever was moved over the crystal at a constant speed of 15 μm s^{-1} guided by an optical microscope. The cantilever was held on the crystal surface at a constant force of 800 nN. Then, the cantilever was retracted and moved to another spot for the next cycle. The indentation fit was performed using an Igor custom-written program and manually checked after the fitting was complete. The curves were then fitted manually. Each approaching force−deformation curve was fitted in the range of 10 nm from the contact point, or from the maximum indentation depth to the contact point if the former was less than 10 nm. By fitting the approaching curve to the Hertz model (1), we could obtain the Young's modulus of the crystals. Typically, three to four such regions (5 μm × 5 μm, 400 pixels) were randomly selected on each crystal to construct the elasticity histogram.

$$F(h) = \frac{2}{\pi} \tan \alpha \frac{E}{1 - \nu^2} h^2 \quad (1)$$

where F is the stress of the cantilever, h is the depth of the crystal pressed by the cantilever tip, α is the half-angle of the tip, E is the Young's modulus of the crystal, and ν is the Poisson ratio. We chose ν = 0.3 in our calculations.

Point Stiffness Calculations. The measured point stiffness (k_{meas}) is composed of the stiffness constants of the cantilever (k_{can}) and the crystals (k_{cry}). Assuming that the crystal and the cantilever act as two springs oriented in a series, the point stiffness of the crystal could be calculated using the following relation: Using eq 2 and an average measured value for k_{meas}, the average stiffness of the crystal could be calculated. To estimate the material property of the crystals, it was assumed that the mechanical behavior of the crystal could be described as linear elastic, which is a good approximation for solids under small strains.

$$k_{cry} = \frac{k_{can} \cdot k_{meas}}{k_{can} - k_{meas}} \quad (2)$$

Brunauer−Emmett−Teller (BET) Surface Area Analysis. The N_2 adsorption isotherm was undertaken at 77 K using a Micromeritics 3Flex instrument.

Computational Optimization of the diPNA-GC Crystal Structure. Calculations were carried out using the Vienna Ab initio Simulation Package VASP 5.3 within the framework of density functional theory (DFT).[55,56] The projector augmented-wave (PAW) method was applied to treat both core and valence electrons.[56] The Kohn−Sham equations[57,58] were solved using a plane-wave basis set, with an energy cutoff of 600 eV. The Perdew−Burke−Ernzerhof (PBE) generalized gradient approximation (GGA) exchange-correlation functional[59] was used. However, to correct for underestimation in band gap prediction when using PBE, calculations using the range-separated hybrid Heyd−Scuseria−Ernzerhof (HSE) functional,[60] with a range-separation μ of 0.11 $Bohr^{-1}$ (HSE06),[61] were carried out. The GGA optPBE functional[62] was used to account for London dispersion. All atomic geometries were fully relaxed until forces were less than 0.01 eV $Å^{-1}$. 2 × 2 × 2 κ-point sampling was used for the triclinic cell and a Gaussian smearing width of 0.05 eV was used for κ space integrals.

UV−Vis Absorption Spectroscopy. UV−vis spectra were measured using a V-550 (JASCO Inc. Japan) spectrophotometer. The cuvette width was 1 cm, and the bandwidth was set at 0.2 nm.

Preparation of the Suprahelical Frameworks/Ruthenium-Complex-Coated Indium Tin Oxide (ITO). The crystals dispersed in water (5.0 mg mL^{-1}) were dropped on the ITO and dried under N_2 for 8 h. Ruthenium solution (1.0 mg mL^{-1}) was then dropped on the crystal-coated ITO and dried under N_2 for another 8 h.

Photocurrent Measurement. The suprahelical frameworks and ruthenium-complex-coated ITO glass slide were incubated in phosphate buffer (100.0 mM, pH 6.0) containing 15% (w/v) TEOA as an electron donor and periodically illuminated with visible light from a 350 W Xe lamp. The photocurrent was measured using an electrochemical workstation under a working voltage of 1.2 V. The ITO glass slide coated with ruthenium complex alone was used as a control.

Cyclic Voltammogram (CV). The suprahelical framework-coated glassy carbon electrode was placed in an electrolytic cell containing 1.0 mg mL^{-1} $Ru(bpy)_3Cl_2$. A 3-electrode system was used to obtain cyclic voltammogram: the crystal-modified glassy carbon (working electrode), Ag/AgCl (reference electrode), and a platinum wire (counter electrode). The cyclic voltammetry curves of $Ru(bpy)_3Cl_2$ were obtained using a scanning rate of 100.0 mV s^{-1} and constant illumination of visible light from a Xe lamp.

Visible Light-Driven NADH Regeneration. First, a film of platinum nanoparticles (Pt NPs), approximately 25 nm thick, was coated on the ITO by evaporation. Photochemical regeneration of NADH was performed in a quartz reactor at room temperature. 1.0 mM NAD^+ was dissolved in phosphate buffer (100.0 mM, pH 6.0) containing 15% (w/v) TEOA. The Pt NPs-sputtered suprahelical frameworks-coated glass slide was then dispersed in the reaction solution and exposed to visible light from a Xe lamp. The concentration of regenerated NADH was calculated based on the absorbance at 340 nm using a spectrophotometer (JASCO, Tokyo, Japan). As a control, only ruthenium complex and Pt NPs were coated on the ITO and the regeneration of NADH was performed and measured as described above. For sustainability study, the diPNA-**GC**-based photosynthesis system was removed from the solution, rinsed clean with water, and then immersed in another reaction cell.

Powder X-ray Diffraction (PXRD). The PXRD patterns were recorded with a Bruker D8 diffractometer using Cu $K\alpha_1$ (λ = 1.5405 Å) radiation with a step of 0.02 at a scanning speed of 8 s per step.

Hirshfeld Surface Analysis. Fingerprint plots of Hirshfeld surfaces were drawn using the CrystalExplorer software.[63]

■ ASSOCIATED CONTENT

Supporting Information

The Supporting Information is available free of charge at https://pubs.acs.org/doi/10.1021/acsami.0c13295.

MS spectrum of the synthesized diPNA-**GC** (Figure S1); reversed-phase high-performance liquid chromatography (HPLC) profile of the synthesized diPNA-**GC** (Figure S2); crystallographic structures of the dipeptides and diPNA crystals (Figure S3); morphological and cavity characterization of the supramolecular frameworks assembled by IV (Figure S4); crystallographic packing of FF self-assembling frameworks (Figure S5); molecular structures of VV assembling frameworks (Figure S6); molecular structures of IV assembling frameworks (Figure S7); crystallographic structures of the LV supramolecular frameworks (Figure S8); magnified representation of the hydrogen bonding network (Figure S9); Hirshfeld surface and the 2-D fingerprint plot (Figures S10 and S12); packing structures of the diPNA-GC supramolecular frameworks (Figure S11); statistical Young's modulus distribution of the bioinspired suprahelical frameworks (Figure S13); statistical point stiffness distribution of the bioinspired suprahelical frameworks (Figure S14); SEM images and XRD spectra (Figure S15); XRD characterizations of the original diPNA-GC frameworks (Figure S16); fluorescence microscopy images of the diPNA-GC self-assembling suprahelical frameworks (Figure S17); comparison of the artificial photosynthesis systems using the amide-based suprahelical frameworks as scaffolds (Figure S18); dipeptide/diPNA sequences examined in this work and their crystal structure parameters (Table S1); and apparent porous parameters of the bioinspired suprahelical frameworks (Table S2) (PDF)

https://dx.doi.org/10.1021/acsami.0c13295
ACS Appl. Mater. Interfaces 2020, 12, 45192−45201

AUTHOR INFORMATION

Corresponding Authors

Kai Tao − *State Key Laboratory of Fluid Power and Mechatronic Systems & Key Laboratory of Advanced Manufacturing Engineering of Zhejiang Province, School of Mechanical Engineering, Zhejiang University, Hangzhou 310027, China;* orcid.org/0000-0003-3899-5181; Email: kai.tao@zju.edu.cn

Bin Xue − *National Laboratory of Solid State Microstructure, Department of Physics, Nanjing University, Nanjing 210093, Jiangsu, China*; Email: xuebinnju@nju.edu.cn

Ehud Gazit − *School of Molecular Cell Biology and Biotechnology, George S. Wise Faculty of Life Sciences, Tel Aviv University, 6997801 Tel Aviv, Israel;* orcid.org/0000-0001-5764-1720; Email: ehudg@post.tau.ac.il

Authors

Shuyi Han − *China Petroleum Engineering & Construction Corp. Southwest Company, Chengdu 610094, Sichuan, China*

Ruth Aizen − *School of Molecular Cell Biology and Biotechnology, George S. Wise Faculty of Life Sciences, Tel Aviv University, 6997801 Tel Aviv, Israel*

Linda J. W. Shimon − *Department of Chemical Research Support, Weizmann Institute of Science, Rehovot 7610001, Israel;* orcid.org/0000-0002-7861-9247

Zhengyu Xu − *National Laboratory of Solid State Microstructure, Department of Physics, Nanjing University, Nanjing 210093, Jiangsu, China*

Yi Cao − *National Laboratory of Solid State Microstructure, Department of Physics, Nanjing University, Nanjing 210093, Jiangsu, China;* orcid.org/0000-0003-1493-7868

Deqing Mei − *State Key Laboratory of Fluid Power and Mechatronic Systems & Key Laboratory of Advanced Manufacturing Engineering of Zhejiang Province, School of Mechanical Engineering, Zhejiang University, Hangzhou 310027, China*

Wei Wang − *National Laboratory of Solid State Microstructure, Department of Physics, Nanjing University, Nanjing 210093, Jiangsu, China;* orcid.org/0000-0001-5441-0302

Complete contact information is available at: https://pubs.acs.org/10.1021/acsami.0c13295

Author Contributions

K.T. and B.X. contributed equally. The manuscript was written through contributions of all authors. All authors have given approval to the final version of the manuscript.

Notes

The authors declare no competing financial interest.

ACKNOWLEDGMENTS

This work was supported in part by the European Research Council under the European Union Horizon 2020 research and innovation program (no. 694426) (E.G.), Joint NSFC-ISF Grant (no. 3145/19) (E.G.), National Natural Science Foundation of China (no.11804148) (B.X.), Natural Science Foundation of Jiangsu province (no. BK20180320) (B.X.), and the Fundamental Research Funds for the Central Universities (no. 020414380118) (B.X.). The authors thank Dr. Ruth Pachter and Dr. Jie Jiang for the band gap calculation assistance, Dr. Sigal Rencus-Lazar for language editing, and the members of Gazit and Cao laboratories for helpful discussions.

REFERENCES

(1) Diercks, C. S.; Yaghi, O. M. The Atom, the Molecule, and the Covalent Organic Framework. *Science* **2017**, *355*, No. eaal1585.

(2) Davis, M. E. Ordered Porous Materials for Emerging Applications. *Nature* **2002**, *417*, 813−821.

(3) Furukawa, H.; Cordova, K. E.; O'Keeffe, M.; Yaghi, O. M. The Chemistry and Applications of Metal-Organic Frameworks. *Science* **2013**, *341*, No. 1230444.

(4) Horike, S.; Shimomura, S.; Kitagawa, S. Soft Porous Crystals. *Nat. Chem.* **2009**, *1*, 695−704.

(5) Li, J.-R.; Kuppler, R. J.; Zhou, H.-C. Selective Gas Adsorption and Separation in Metal-Frameworks. *Chem. Soc. Rev.* **2009**, *38*, 1477−1504.

(6) Lin, R. B.; He, Y.; Li, P.; Wang, H.; Zhou, W.; Chen, B. L. Multifunctional Porous Hydrogen-Bonded Organic Framework Materials. *Chem. Soc. Rev.* **2019**, *48*, 1362−1389.

(7) Ma, Y.; Tong, W.; Zhou, H.; Suib, S. L. A Review of Zeolite-Like Porous Materials. *Microporous Mesoporous Mater.* **2000**, *37*, 243−252.

(8) Zhou, H.-C.; Long, J. R.; Yaghi, O. M. Introduction to Metal-Organic Frameworks. *Chem. Rev.* **2012**, *112*, 673−674.

(9) Shen, K.; Zhang, L.; Chen, X.; Liu, L.; Zhang, D.; Han, Y.; Chen, J.; Long, J.; Luque, R.; Li, Y.; Chen, B. L. Ordered Macro-Microporous Metal-Organic Framework Single Crystals. *Science* **2018**, *359*, 206−210.

(10) Snurr, R. Q. It's an Interesting MOF, but Is It Stable? *Matter* **2019**, *1*, 26−27.

(11) He, Y.; Xiang, S.; Chen, B. L. A Microporous Hydrogen-Bonded Organic Framework for Highly Selective C_2H_2/C_2H_4 Separation at Ambient Temperature. *J. Am. Chem. Soc.* **2011**, *133*, 14570−14573.

(12) Luo, X. Z.; Jia, X. J.; Deng, J. H.; Zhong, J. L.; Liu, H. J.; Wang, K. J.; Zhong, D. C. A Microporous Hydrogen-Bonded Organic Framework: Exceptional Stability and Highly Selective Adsorption of Gas and Liquid. *J. Am. Chem. Soc.* **2013**, *135*, 11684−11687.

(13) Wang, H.; Li, B.; Wu, H.; Hu, T. L.; Yao, Z.; Zhou, W.; Xiang, S.; Chen, B. L. A Flexible Microporous Hydrogen-Bonded Organic Framework for Gas Sorption and Separation. *J. Am. Chem. Soc.* **2015**, *137*, 9963−9970.

(14) Anderson, S. L.; Boyd, P. G.; Gładysiak, A.; Nguyen, T. N.; Palgrave, R. G.; Kubicki, D.; Emsley, L.; Bradshaw, D.; Smit, M. J.; Stylianou, K. C.; Rosseinsky, B. Nucleobase Pairing and Photodimerization in a Biologically Derived Metal-Organic Framework Nanoreactor. *Nat. Commun.* **2019**, *10*, No. 1612.

(15) Stylianou, K. C.; Warren, J. E.; Chong, S. Y.; Rabone, J.; Bacsa, J.; Bradshaw, D.; Rosseinsky, M. J. CO_2 Selectivity of a 1D Microporous Adenine-Based Metal−Organic Framework Synthesized in Water. *Chem. Commun.* **2011**, *47*, 3389−3391.

(16) Rabone, J.; Yue, Y.-F.; Chong, S.; Stylianou, K. C.; Bacsa, J.; Bradshaw, D.; Darling, G. R.; Berry, N. G.; Khimyak, Y. Z.; Ganin, A. Y.; Wiper, P.; Claridge, J. B.; Rosseinsky, M. J. An Adaptable Peptide-Based Porous Material. *Science* **2010**, *329*, 1053−1057.

(17) Katsoulidis, A. P.; Antypov, D.; Whitehead, G. F. S.; Carrington, E. J.; Adams, D. J.; Berry, N. G.; Darling, G. R.; Dyer, M. S.; Rosseinsky, M. J. Chemical Control of Structure and Guest Uptake by a Conformationally Mobile Porous Material. *Nature* **2019**, *565*, 213−217.

(18) Katsoulidis, A. P.; Park, K. S.; Antypov, D.; Martí-Gastaldo, C.; Miller, G. J.; Warren, J. E.; Robertson, C. M.; Blanc, F.; Darling, G. R.; Berry, N. G.; Purton, J. A.; Adams, D. J.; Rosseinsky, M. J. Guest-Adaptable and Water-Stable Peptide-Based Porous Materials by Imidazolate Side Chain Control. *Angew. Chem., Int. Ed.* **2014**, *53*, 193−198.

(19) Bracco, S.; Asnaghi, D.; Negroni, M.; Sozzani, P.; Comotti, A. Porous Dipeptide Crystals as Volatile-Drug Vessels. *Chem. Commun.* **2018**, *54*, 148−151.

(20) Görbitz, C. H. Microporous Organic Materials from Hydrophobic Dipeptides. *Chem. - Eur. J.* **2007**, *13*, 1022−1031.

(21) Görbitz, C. H. Nanotube Formation by Hydrophobic Dipeptides. *Chem. - Eur. J.* **2001**, *7*, 5153−5159.

(22) Görbitz, C. H. The Structure of Nanotubes Formed by Diphenylalanine, the Core Recognition Motif of Alzheimer's β-Amyloid Polypeptide. *Chem. Commun.* **2006**, 2332−2334.
(23) Tao, K.; Makam, P.; Aizen, R.; Gazit, E. Self-Assembling Peptide Semiconductors. *Science* **2017**, *358*, No. eaam9756.
(24) Tao, K.; Wang, J.; Zhou, P.; Wang, C.; Xu, H.; Zhao, X.; Lu, J. R. Self-Assembly of Short Aβ(16-22) Peptides: Effect of Terminal Capping and the Role of Electrostatic Interaction. *Langmuir* **2011**, *27*, 2723−2730.
(25) Spackman, M. A.; Jayatilaka, D. Hirshfeld Surface Analysis. *CrystEngComm* **2009**, *11*, 19−32.
(26) Berger, O.; Gazit, E. Molecular Self-Assembly Using Peptide Nucleic Acids. *Pept. Sci.* **2017**, *108*, No. e22930.
(27) Egholm, M.; Buchardt, O.; Nielsen, P. E.; Berg, R. H. Peptide Nucleic Acids (PNA). Oligonucleotide Analogs with an Achiral Peptide Backbone. *J. Am. Chem. Soc.* **1992**, *114*, 1895−1897.
(28) Buchardt, O.; Egholm, M.; Nielsen, P. E.; Berg, R. H. Peptide Nucleic Acids Having Amino Acid Side Chains. U.S. Patent US5,719,262A,1998.
(29) Berger, O.; Adler-Abramovich, L.; Levy-Sakin, M.; Grunwald, A.; Liebes-Peer, Y.; Bachar, M.; Buzhansky, L.; Mossou, E.; Forsyth, V. T.; Schwartz, T.; Ebenstein, Y.; Frolow, F.; Shimon, L. J. W.; Patolsky, F.; Gazit, E. Light-Emitting Self-Assembled Peptide Nucleic Acids Exhibit Both Stacking Interactions and Watson-Crick Base Pairing. *Nat. Nanotechnol.* **2015**, *10*, 353−360.
(30) Gao, J.; Zhang, W.; Wu, Z.; Zheng, Y.; Fu, D. Enantiomorphic Perovskite Ferroelectrics with Circularly Polarized Luminescence. *J. Am. Chem. Soc.* **2020**, *142*, 4756−4761.
(31) Gan, Z.; Wu, X.; Zhu, X.; Shen, J. Light-Induced Ferroelectricity in Bioinspired Self-Assembled Diphenylalanine Nanotubes/Microtubes. *Angew. Chem., Int. Ed.* **2013**, *52*, 2055−2059.
(32) Tao, K.; Xue, B.; Li, Q.; Hu, W.; Shimon, L. J. W.; Makam, P.; Si, M.; Yan, X.; Zhang, M.; Cao, Y.; Yang, R. S.; Li, J. B.; Gazit, E. Stable and Optoelectronic Dipeptide Assemblies for Power Harvesting. *Mater. Today* **2019**, *30*, 10−16.
(33) Knowles, T. P.; Fitzpatrick, A. W.; Meehan, S.; Mott, H. R.; Vendruscolo, M.; Dobson, C. M.; Welland, M. E. Role of Intermolecular Forces in Defining Material Properties of Protein Nanofibrils. *Science* **2007**, *318*, 1900−1903.
(34) Herling, T. W.; Garcia, G. A.; Michaels, T. C.; Grentz, W.; Dean, J.; Shimanovich, U.; Gang, H.; Müller, T.; Kav, B.; Terentjev, E. M.; Dobson, C. M.; Knowles, T. P. J. Force Generation by the Growth of Amyloid Aggregates. *Proc. Natl. Acad. Sci. U.S.A.* **2015**, *112*, 9524−9529.
(35) Tao, K.; Hu, W.; Xue, B.; Chovan, D.; Brown, N.; Shimon, L. J. W.; Maraba, O.; Cao, Y.; Tofail, S. A.; Thompson, D.; Li, J. B.; Yang, R. S.; Gazit, E. Bioinspired Stable and Photoluminescent Assemblies for Power Generation. *Adv. Mater.* **2019**, *31*, No. 1807481.
(36) Knowles, T. P.; Buehler, M. J. Nanomechanics of Functional and Pathological Amyloid Materials. *Nat. Nanotechnol.* **2011**, *6*, 469−479.
(37) Zelenovskiy, P.; Kornev, I.; Vasilev, S.; Kholkin, A. On the Origin of the Great Rigidity of Self-Assembled Diphenylalanine Nanotubes. *Phys. Chem. Chem. Phys.* **2016**, *18*, 29681−29685.
(38) Zhao, Y.; Ge, Z.; Fang, J. Elastic Modulus of Viral Nanotubes. *Phys. Rev. E* **2008**, *78*, No. 031914.
(39) Xu, Z.; Paparcone, R.; Buehler, M. J. Alzheimer's Aβ(1-40) Amyloid Fibrils Feature Size-Dependent Mechanical Properties. *Biophys. J.* **2010**, *98*, 2053−2062.
(40) Yogurtcu, O. N.; Wolgemuth, C. W.; Sun, S. X. Mechanical Response and Conformational Amplification in α-Helical Coiled Coils. *Biophys. J.* **2010**, *99*, 3895−3904.
(41) López-García, P.; Goktas, M.; Bergues-Pupo, A. E.; Koksch, B.; Silva, D. V.; Blank, K. G. Structural Determinants of Coiled Coil Mechanics. *Phys. Chem. Chem. Phys.* **2019**, *21*, 9145−9149.
(42) Bera, S.; Mondal, S.; Xue, B.; Shimon, L. J. W.; Cao, Y.; Gazit, E. Rigid helical-like assemblies from a self-aggregating tripeptide. *Nat. Mater.* **2019**, *18*, 503−509.
(43) Baimpos, T.; Nikolakis, V.; Kouzoudis, D. Measurement of the Elastic Properties of Zeolite Films Using Metglas-Zeolite Composite Sensors. *Stud. Surf. Sci. Catal.* **2008**, *174*, 665−668.
(44) Tan, J. C.; Cheetham, A. K. Mechanical Properties of Hybrid Inorganic-Organic Framework Materials: Establishing Fundamental Structure-Property Relationships. *Chem. Soc. Rev.* **2011**, *40*, 1059−1080.
(45) Rogge, S. M. J.; Waroquier, M.; Speybroeck, V. V. Reliably Modeling the Mechanical Stability of Rigid and Flexible Metal-Organic Frameworks. *Acc. Chem. Res.* **2018**, *51*, 138−148.
(46) Ortiz, A. U.; Boutin, A.; Fuchs, A. H.; Coudert, F.-X. Anisotropic Elastic Properties of Flexible Metal-Organic Frameworks: How Soft are Soft Porous Crystals? *Phys. Rev. Lett.* **2012**, *109*, No. 195502.
(47) Nikitin, T.; Kopyl, S.; Shur, V. Y.; Kopelevich, Y. V.; Kholkin, A. L. Low-Temperature Photoluminescence in Self-Assembled Diphenylalanine Microtubes. *Phys. Lett. A* **2016**, *380*, 1658−1662.
(48) Amdursky, N.; Beker, P.; Koren, I.; Bank-Srour, B.; Mishina, E.; Semin, S.; Rasing, T.; Rosenberg, Y.; Barkay, Z.; Gazit, E.; Rosenman, G. Structural Transition in Peptide Nanotubes. *Biomacromolecules* **2011**, *12*, 1349−1354.
(49) Tao, K.; Donnell, J. O'.; Yuan, H.; Haq, E. U.; Guerin, S.; Shimon, L. J. W.; Xue, B.; Silien, C.; Cao, Y.; Thompson, D.; Yang, R.; Tofail, S. A. M.; Gazit, E. Accelerated Charge Transfer in Water-Layered Peptide Assemblies. *Energy Environ. Sci.* **2020**, *13*, 96−101.
(50) Tao, K.; Xue, B.; Frere, S.; Slutsky, I.; Cao, Y.; Wang, W.; Gazit, E. Multiporous Supramolecular Microspheres for Artificial Photosynthesis. *Chem. Mater.* **2017**, *29*, 4454−4460.
(51) Tao, K.; Fan, Z.; Sun, L.; Makam, P.; Tian, Z.; Ruegsegger, M.; Shaham-Niv, S.; Hansford, D.; Aizen, R.; Pan, Z.; Galster, S.; Ma, J.; Yuan, F.; Su, M.; Qu, S.; Zhang, M.; Gazit, E.; Li, J. B. Quantum Confined Peptide Assemblies with Tunable Visible to Near-Infrared Spectral Range. *Nat. Commun.* **2018**, *9*, No. 3217.
(52) Kim, S.; Kim, J. H.; Lee, J. S.; Park, C. B. Beta-Sheet-Forming, Self-Assembled Peptide Nanomaterials towards Optical, Energy, and Healthcare Applications. *Small* **2015**, *11*, 3623−3640.
(53) Sun, B.; Tao, K.; Jia, Y.; Yan, X.; Zou, Q.; Gazit, E.; Li, J. B. Photoactive Properties of Supramolecular Assembled Short Peptides. *Chem. Soc. Rev.* **2019**, *48*, 4387−4400.
(54) Lee, S. H.; Kim, J. H.; Park, C. B. Coupling Photocatalysis and Redox Biocatalysis toward Biocatalyzed Artificial Photosynthesis. *Chem. - Eur. J.* **2013**, *19*, 4392−4406.
(55) Kresse, G.; Furthmüller, J. Efficiency of Ab-Initio Total Energy Calculations for Metals and Semiconductors Using a Plane-Wave Basis Set. *Comput. Mater. Sci.* **1996**, *6*, 15−50.
(56) Kresse, G.; Joubert, D. From Ultrasoft Pseudopotentials to the Projector Augmented-Wave Method. *Phys. Rev. B* **1999**, *59*, 1758.
(57) Hohenberg, P.; Kohn, W. Inhomogeneous Electron Gas. *Phys. Rev.* **1964**, *136*, B864.
(58) Kohn, W.; Sham, L. J. Self-Consistent Equations Including Exchange and Correlation Effects. *Phys. Rev.* **1965**, *140*, A1133.
(59) Perdew, J. P.; Burke, K.; Ernzerhof, M. Generalized Gradient Approximation Made Simple. *Phys. Rev. Lett.* **1996**, *77*, 3865.
(60) Heyd, J.; Scuseria, G. E.; Ernzerhof, M. Hybrid Functionals Based on a Screened Coulomb Potential. *J. Chem. Phys.* **2003**, *118*, No. 8207.
(61) Krukau, A. V.; Vydrov, O. A.; Izmaylov, A. F.; Scuseria, G. E. Influence of the Exchange Screening Parameter on the Performance of Screened Hybrid Functionals. *J. Chem. Phys.* **2006**, *125*, No. 224106.
(62) Klimeš, J.; Bowler, D. R.; Michaelides, A. Van der Waals Density Functionals Applied to Solids. *Phys. Rev. B* **2011**, *83*, No. 195131.
(63) Turner, M. J.; McKinnon, J. J.; Wolff, S. K.; Grimwood, D. J.; Spackman, P. R.; Jayatilaka, D.; Spackman, M. A. *CrystalExplorer17*; University of Western Australia. http://hirshfeldsurface.net., 2017.

https://dx.doi.org/10.1021/acsami.0c13295
ACS Appl. Mater. Interfaces 2020, 12, 45192−45201